Multiple Giant-Magnetoresistance Sensors Controlled by Additive Dipolar Coupling

J. Torrejon,[*,‡] A. Solignac, C. Chopin, J. Moulin, A. Doll, E. Paul, C. Fermon, and M. Pannetier-Lecoeur[†]

Université Paris-Saclay, CEA, CNRS, SPEC, 91191 Gif-Sur-Yvette, France

(Received 19 November 2019; revised manuscript received 23 January 2020; accepted 13 February 2020; published 12 March 2020)

Vertical packaging of multiple giant magnetoresistance (multi-GMR) stacks is a very interesting noise reduction strategy for local magnetic sensor measurements, which has not been reported experimentally so far. Here, we fabricate multi-GMR sensors (up to 12 repetitions) that maintain a good GMR ratio, linearity, and low roughness. From magnetotransport measurements, two different resistance responses are observed with a crossover at around five GMR repetitions: steplike ($N < 5$) and linear ($N \geq 5$) behavior, respectively. With the help of micromagnetic simulations, we analyze, in detail, the two main magnetic mechanisms: the Néel coupling distribution induced by the roughness propagation and the additive dipolar coupling between the N free layers. Furthermore, we correlate the dipolar coupling mechanism, which is controlled by the number of GMRs (N) and lateral dimensions (width), to the sensor performance (sensitivity, noise, and detectivity); this is in good agreement with analytical theory. The noise roughly decreases in multi-GMRs as $1/\sqrt{N}$ in both regimes (low-frequency $1/f$ and thermal noise). The sensitivity is even more strongly reduced, scaling as N^{-1}, in the strong dipolar regime (narrow devices), while converging to a constant value in the weak dipolar regime (wide devices). Interestingly, they are more robust against undesirable random telegraphic noise than single GMRs at high voltages, and the linearity can be extended towards a much larger magnetic field range, without dealing with the size and reduction of the GMR ratio. Finally, we identify the optimal conditions for which multi-GMRs exhibit lower magnetic field detectivity than that of single GMRs: wide devices operating in the thermal regime, where much higher voltage can be applied without generating remarkable magnetic noise. These results open the path towards spintronics sensors connected and coupled in three dimensions with reduced noise, compact footprint, and mainly tuned by the dipolar coupling.

DOI: 10.1103/PhysRevApplied.13.034031

I. INTRODUCTION

Spintronic devices based on giant-magnetoresistance (GMR) [1,2] exhibit large magnetoresistance variation, which have been extensively used to read the magnetic information contained in hard disks during the last decades. In recent years, GMR devices have also opened the market to weak magnetic sensing applications [3], mainly in automotive [4] or biological [5,6] systems, thanks to the remarkable enhancement in quality, in terms of signal-to-noise ratio and CMOS compatibility, allowing small-size integrated devices. Nevertheless, the strong correlation between magnetic field detection and sensor size is nowadays the main barrier to developing higher performance sensors at the micro- and nanoscale. Moreover, the detectivity in these devices is often limited by the presence of $1/f$ low-frequency magnetic noise or random telegraphic noise (RTN) due to domain fluctuations in the sensing magnetic layer [7–9]. Several noise reduction schemes have been explored to mitigate these constrains, ranging from sensors coupled to flux concentrators [10], MR sensors connected in series [11] or applying pinning in the sensing layer [9,12–16]. But, very often, such schemes have the disadvantage of increasing the footprint device and resistance (and consequently, thermal noise) and reducing the spatial resolution, which is critical for local measurements.

An innovative strategy to reduce the noise, without dealing with the lateral size, is to connect vertically GMRs that combine low-frequency noise and low resistance, while maintaining a compact footprint. Vertical packaging systems, based on several spin valves stacked on top of each other and separated by a thick insulator spacer, have been theoretically proposed [17], but never experimentally demonstrated. One of the main challenges is related to

*jacob.torrejon-diaz@curie.fr

†myriam.pannetier-lecoeur@cea.fr

‡Present address: Institut Curie, PSL Research University, CNRS UMR, INSERM, Orsay, France.

the thick insulator spacer (SiO_2, AlO*x*, etc.), which should minimize the magnetostatic coupling, while maintaining a low roughness.

Here, we fabricate multi-GMR stacks (up to 12 repetitions) separated by a thin Ta spacer with low roughness, analyze the main reversal magnetization mechanisms (Dipolar versus Néel couplings), successfully demonstrate noise reduction (in the $1/f$ and thermal regimes), and finally identify the optimal conditions towards lower magnetic field detectivity.

The paper is organized as follows. In Sec. II, we first introduce the experimental methods: sensor fabrication (sputtering, optical lithography, and Ar-ion etching), magnetotransport and noise setups, and micromagnetic simulation details. We then present in Secs. III and IV the magnetoresistance study in unpatterned multi-GMR thin films and yoke-shaped sensors, respectively, quantifying the role of Néel and dipolar couplings with the help of micromagnetic simulations. In Sec. IV, finally, we evaluate the multi-GMR sensor performance parameters (sensitivity, noise, and detectivity) as a function of number of GMRs, width and input voltage, and the correlation with the dipolar coupling mechanism.

II. METHODS

A. Experimental details

Multi-GMR stacks are deposited by sputtering on thermally oxidized (500 nm SiO_2) silicon wafers. Stacks comprise a generic top-pinned synthetic antiferromagnetic (SAF) spin-valve sequence [$Ni_{89}Fe_{19}$(5)/$Co_{90}Fe_{10}$(2.1) / Cu(2.9) / $Co_{90}Fe_{10}$(2.1) / Ru(0.85) / $Co_{90}Fe_{10}$(2) / $Ir_{80}Mn_{20}$(7.5)] repeated N times [Fig. 1(a)], with N being varied from 1 to 12. Thicknesses are given in nm. The bottom free layer is composed of the Ni-Fe/Co-Fe bilayer, while the top pinned layer is a synthetic antiferromagnet, Co-Fe/Ru/Co-Fe/Ir-Mn. The multi-GMR stack is deposited onto a 3 nm Ta seed layer and ends with a Ru(0.4)/Ta(5) capping bilayer. For $N > 1$, each top spin-valve sequence is separated from the next one by a 3-nm thick Ta layer, which allows dipolar coupling between the free layers, while maintaining a low roughness. After deposition, stacks are annealed under vacuum for 1 h at 473 K in a 1 T field applied in plane to set the pinned-layer magnetization. Two thin-film sets with nominally the same composition are deposited at different dates: first, film set A for the preliminary optimization of the multi-GMR stack

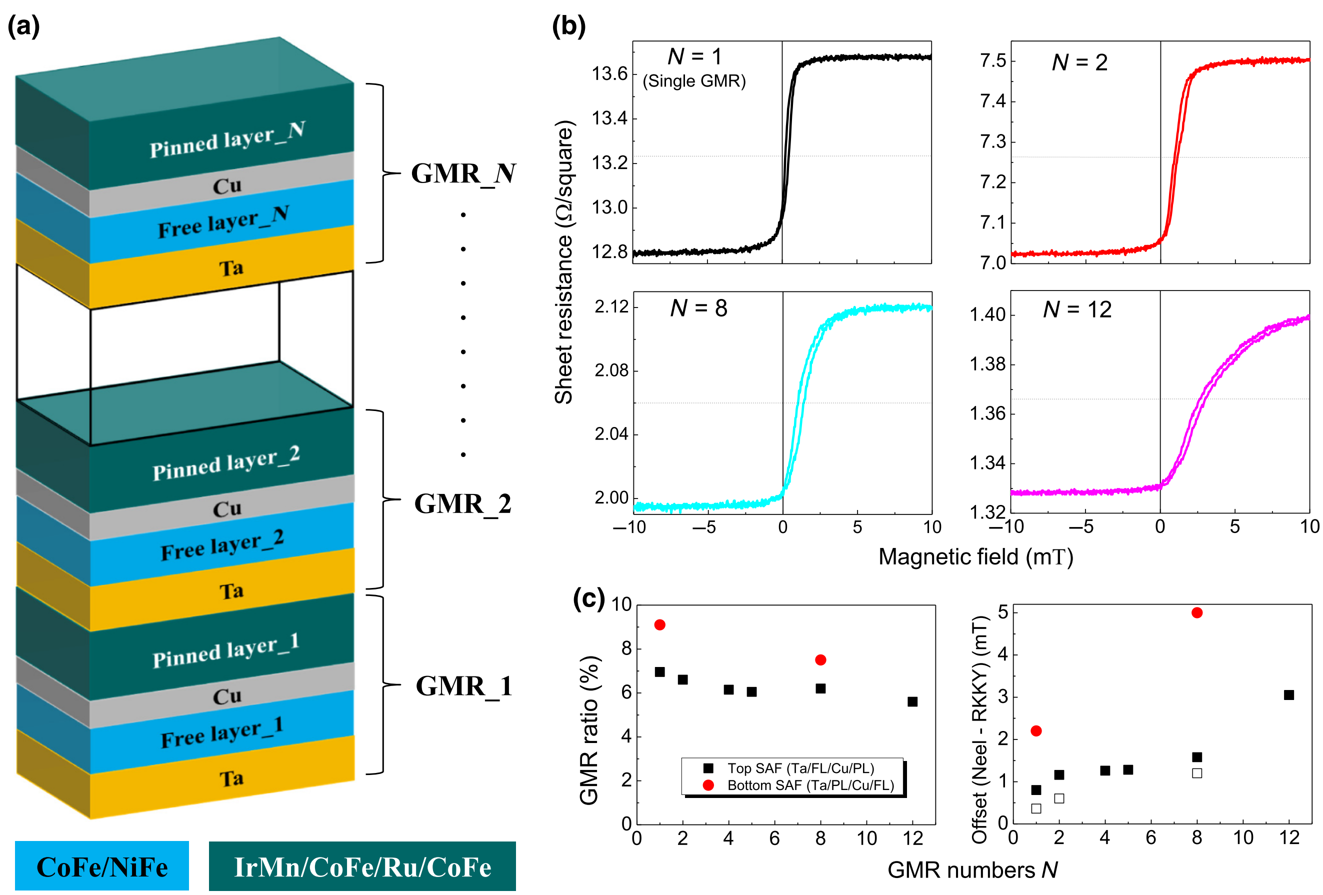

FIG. 1. Magnetoresistance in multi-GMR thin films. (a) Scheme of multi-GMR thin films based on several repetitions of top-SAF spin valves. (b) *R-H* curves for 1, 2, 8, and 12 GMRs. (c) GMR ratio Δ_{GMR} and offset evolution with the GMR number. FL, free layer; PL, pinned layer. Solid (open) black squares corresponds to film set B (A).

configuration (see more details in Fig. S1 within the Supplemental Material [18]), and then film set B for optimized and patterned multi-GMR sensors. Notably, both exhibit the same GMR ratio Δ_{GMR} and hysteresis, but slightly different horizontal offsets: the offset in film set B is slightly larger (0.3–0.5 mT) than that in film set A [see right panel in Fig. 1(c) for direct comparison].

The stacks are patterned by combining optical lithography and Ar-ion etching of yoke-shaped devices [Fig. 2(a)] [19,20], which favors magnetic domain stabilization inside the main arm of the yoke [21]. Sensor widths vary from 1 to 30 μm, with a constant aspect ratio of 50:1 ($L = 50\,w$), which leads to a nominal single-element resistance, R_1, of 750–800 Ω. Each repetition will therefore theoretically lead to $R_N = R_1/N$. Finally, the yokes are connected in a current-in-plane (CIP) configuration by Ta(5)/Cu(150)/Ta(5) contacts and passivated by a protective 150-nm thick Al_2O_3 layer deposited by sputtering as a last step in the microfabrication process.

Magnetotransport measurements (*R-H* curves) are performed by measuring the dc output voltage using four probes for the unpatterned films and two probes for the

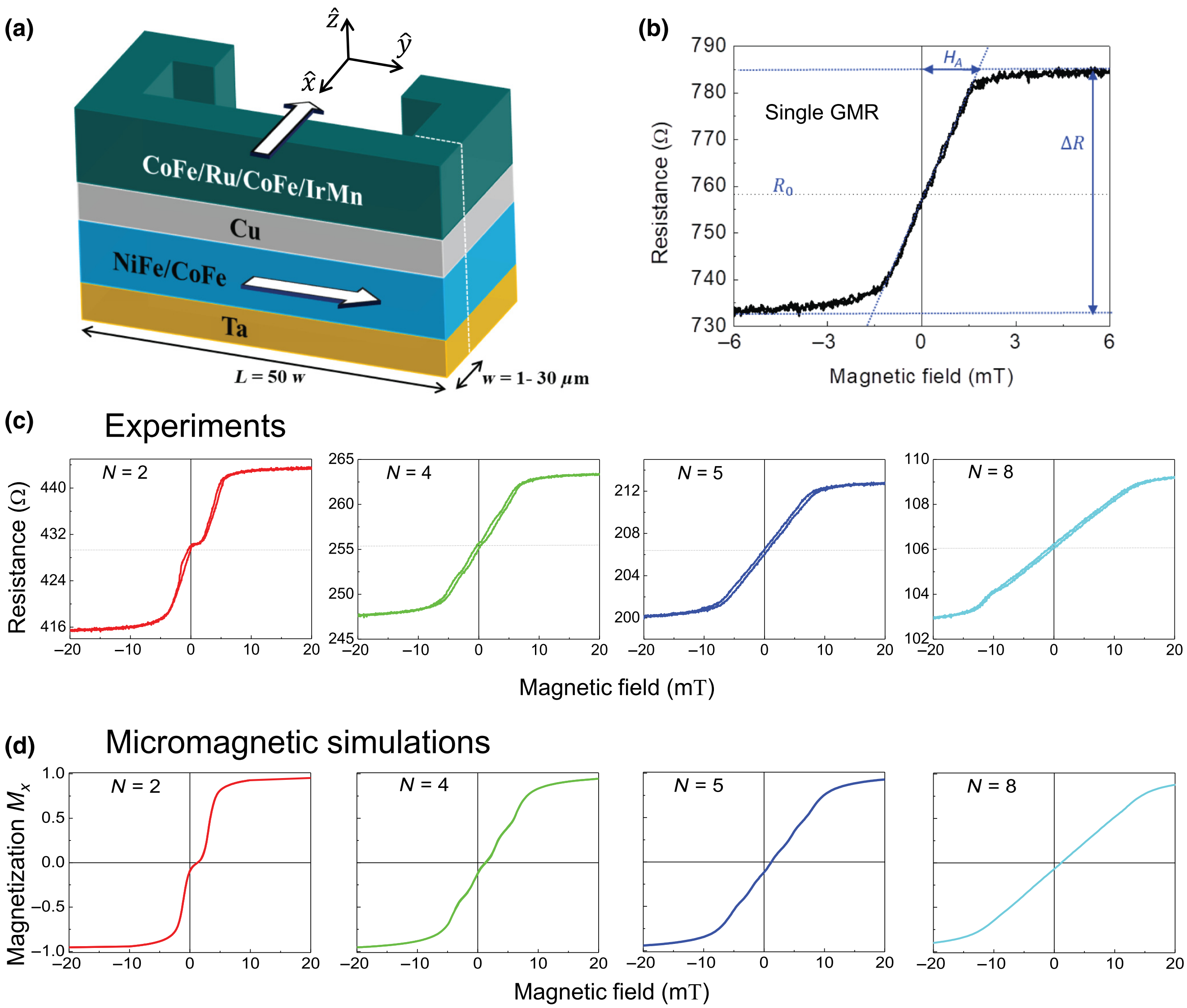

FIG. 2. Magnetoresistance in microdevices: experiments versus simulations. (a) Scheme of yoke-shaped GMR based on Top-SAF spin valves. (b),(c) Experimental *R-H* curves for devices composed of a single GMR device, 2, 4, and 8 GMRs. (d) Magnetization reversal curves computed by OOMMF micromagnetic simulations for N free-layer multistacks, $N = 2,4,5$, and 8. The dimensions of the free layer are a rectangular prism of $200 \times 4 \times 0.007\ \mu\mathrm{m}^3$. We assume that Ni-Fe and Co-Fe layers are perfectly coupled by exchange with the following averaged magnetic parameters: saturation magnetization $M_s = 850$ kA/m, exchange constant $J_s = 10$ pJ/m, weak uniaxial magnetic anisotropy $K_u = 200\ \mathrm{J/m^3}$, and Néel coupling distribution ($H_{n1} = 0.8$ mT, $H_{n2} = 1.3$ mT, $H_{n3} = 1.4$ mT, $H_{n4} = 1.5$ mT, and $H_{n5} = H_{n6} = H_{n7} = H_{n8} = 1.6$ mT). The gap (vertical separation) between consecutive free layers is 28 nm.

yokes in a homemade setup. The external field is varied along the pinned-layer direction (i.e., 90° from the yoke-arm length) through a Helmholtz coil between ±25 mT.

Noise measurements are performed in a magnetically shielded room through power spectrum recordings over the frequency range studied here (1 Hz–3 kHz) [20]. The GMR sensor is biased using a battery through a balanced Wheatstone bridge. The bridge output is amplified by an INA103 low-pass amplifier before a second step of amplification and band-pass filtering. An acquisition card acquires the temporal signal and a fast Fourier transform (FFT) is used to measure the noise spectral density. An ac field signal created by a coil (7 μT_{rms}, 30 Hz) and applied along the sensitivity axis serves as a calibration reference, allowing extraction of the limit of detection in nT.

B. Micromagnetic modeling details

The magnetoresistance response of the multi-GMR sensors in Fig. 2(b) are modeled by OOMMF micromagnetic simulations [22]. The geometry of the free layer is a rectangular prism 7 nm thick, 4 μm wide, and 200 μm long, and the gap between consecutive free layers is 28 nm. We assume that Ni-Fe (5 nm thick) and Co-Fe (2 nm thick) layers are perfectly coupled by direct exchange with the following averaged magnetic parameters: saturation magnetization $M_s = 850$ kA/m, exchange constant $J_s =$ 10 pJ/m, and weak uniaxial magnetic anisotropy $K_u =$ 200 J/m^3. The parameter values are in good agreement with those reported in the literature [23]. The roughness of each free layer induces a Néel coupling (magnetostatic coupling between free layer i and its closest SAF layer that exhibits correlated roughness), which has been included in the simulations as bias field H_{ni} (along the SAF pinned-layer direction fixed during the annealing process). We select values close to the experimental curves in Fig. 1: $H_{n1} = 0.8$ mT, $H_{n2} = 1.3$ mT, $H_{n3} = 1.4$ mT, $H_{n4} = 1.5$ mT, and $H_{n6\text{–}8} = 1.6$ mT). Indeed, we consider, for simplicity, that the growth differences that could appear between the free layers (roughness, magnetization, or thickness changes) are summarized in the Néel coupling. Very small magnetic field misalignment (1°) is applied to break the symmetry between clockwise or anticlockwise magnetization rotation. To summarize, the stable magnetic configuration is given by competition between the Zeeman energy, the magnetocrystalline (MC) and shape anisotropies, and the dipolar and Néel interlayer couplings.

III. MAGNETORESISTANCE OF MULTI-GMRs IN THIN FILMS: THE ROLE OF NÉEL COUPLING VARIATION

First, we characterize and optimize multi-GMR thin films (up to $N = 12$) from magnetoresistance measurements [Figs. 1(b) and 1(c)]. During the optimization process, several multi-GMR combinations are explored: multi-GMRs based on top-SAF spin valves, bottom-SAF spin valves, a combination of both, different spacers (Ta and MgO), etc. (see more details in Fig. S1 within the Supplemental Material [18]). However, use of the bottom-SAF spin valves structure and/or MgO spacer degrades the thin-film stack quality, promoting strong roughness and an offset field. We identify the best multi-GMR in terms of high GMR ratio ($\Delta_{GMR} = 6\%$–7%), good linearity, and low offset (≤ 3 mT for maximum $N = 12$) for a stack composed by N repetitions of top-SAF spin valves, where each single GMR unit (Ni-Fe/Co-Fe/Cu/Co-Fe/Ru/Co-Fe/Ir-Mn) is separated by a 3 nm Ta layer, as shown Fig. 1(a). As N increases, the GMR ratio (measured at maximum field, ±25 mT) decreases very slightly from 7% ($N = 1$) to 6% ($N = 12$), left panel in Fig. 1(c). This is in contrast to single GMRs, where an increase of magnetic volume results in a stronger decrease of the MR ratio. For example, for a single GMR with 15-nm thick Ni-Fe (equivalent roughly to a multi-GMR with N slightly larger than 2), the GMR ratio decays down to 4% and the linearity is strongly degraded (Fig. S2 within the Supplemental Material [18]).

On another hand, the average horizontal offset increases about 0.4 mT from the single to the double GMR stack, but then it remains almost constant until $N = 8$ and the offset increases again up to about 3 mT for the thickest stack with $N = 12$ [right panel in Fig. 1(c)]. The horizontal offset in a single GMR is mainly determined by competition between oscillatory interlayer exchange coupling Ruderman–Kittel–Kasuya–Yosida (RKKY) [24,25] and Néel [26,27] coupling. For optimal sensor performance, the RKKY interaction, which favors an antiparallel (AP) configuration between free and pinned layers, should be likely compensated by Néel coupling, which favors the parallel (P) configuration. The oscillatory RKKY is mainly controlled by the Cu spacer thickness between pinned and free layers, while the Néel coupling depends on the correlated roughness between the free and pinned layers set up by dipoles at the homologous protrusions and bumps at the interfaces. For a single GMR [Fig. 1(b)], we obtain a good offset compensation (between 0.3 and 0.8 mT, for film sets A and B, respectively) for a Cu thickness of 2.9, with 3 nm Ta as a buffer layer, which promotes the lowest roughness GMR stacks. For multi-GMR stacks, the thickness of the Cu layers is kept constant, such that the offset variation is only ascribed to the Néel coupling variation as a consequence of roughness propagation between successive GMRs. The roughness degradation in multi-GMRs is only remarkable between the first and second free layers and for multi-GMRs with $N = 12$, where the linearity also deteriorates. Notably, another multi-GMR system based on inverted bottom-SAF spin valves (Ir-Mn/Co-Fe/Ru/Co-Fe/Cu/Co-Fe/Ni-Fe) exhibits 20%–30% larger GMR ratios, but its offset (roughness) and coercivity are strongly increased up to five times compared with the top-SAF spin valves [Fig. 1(c)].

In general, the increase of the Néel field variation (roughness propagation) in each successive free layer degrades the linear behavior. However, optimized top-SAF multi-GMRs in this study [Figs. 1(b)] exhibit a good linear response because the Néel coupling variation is small relative to the linear magnetic field range for each individual free layer, which is mainly governed by the magnetocrystalline anisotropy, H_{MC}. Here, we assume that H_{MC} does not change between successive free layers, leading to very similar resistance slopes. For nonoptimized multi-GMRs, the Néel coupling variation is much larger, inducing steplike behavior [Fig. S1(a) within the Supplemental Material [18]]. Even very high roughness levels can vary the magnetocrystalline anisotropy in upper free layers to degrade drastically the MR curve.

IV. MAGNETORESISTANCE OF YOKE-SHAPED MULTI-GMR SENSORS: THE ROLE OF ADDITIVE DIPOLAR COUPLING

First, we analyze the magnetoresistance of yoke-shaped multi-GMR sensors as a function of the number of GMR repetitions. Quality control of the multi-GMR sensors devices can be found in Fig. S3 within the Supplemental Material [18], which demonstrates very good fabrication quality (sputtering and microfabrication), and therefore, high reproducibility of the yoke-shaped sensors. Then, we perform micromagnetic simulations to understand and quantify the role of the additive dipolar coupling (magnetostatic field interactions between successive free layers) over the Néel coupling variation (magnetostatic interaction between free and pinned layers with correlated roughness in each individual GMR).

A. Experiments

A linear variation of the GMR resistance with the magnetic field, with a low hysteresis, is obtained when the easy magnetization axis of the free layer is set perpendicular to the pinned layer. This is achieved through the shape anisotropy [28] by patterning the yoke-arm length perpendicular to the pinned-layer magnetization, as shown in Fig. 2(a). The sensor magnetoresistance evolution with the number of GMR repetitions and constant width of $w = 4$ μm is shown in Figs. 2(b) and 2(c). We can clearly identify two different regimes. For $N < 5$, the resistance shows a steplike response, according to the number of repetitions. For $N \geq 5$, the *R*-*H* curve exhibits a linear response. A similar trend is observed when keeping N constant and varying the width (see Fig. S4 within the Supplemental Material [18]). For $N = 2$ ($N = 4$), steplike behavior is observed for $w > 1$ μm ($w > 2$ μm) and linear behavior for $w \leq 1$ μm ($w \leq 2$ μm). Therefore, multi-GMR devices with a large number of GMR and/or narrow sizes promote linear behavior, which is more desirable for sensor applications.

These results indicate a strong effect of dipolar couplings between neighboring GMRs. In multi-GMR sensors, the dipolar fields are mainly governed by the free layers, rather than the pinned layers. The pinned layer is a compensated SAF (with an effective thickness t_{SAF}~0.1 nm) and its dipolar field is typically more than one order of magnitude smaller than that of the free layer ($t_{FL} = 7$ nm). For this reason, in our analysis, we consider only the dipolar fields from the N free layers.

The GMR ratio Δ_{GMR} in yoke-shaped sensors follows the same evolution as that in thin films: The MR ratio slightly decreases from $N = 1$ to $N = 12$ [Fig. 3(a)]. Notably, the decrease in GMR ratio at low width is artificial and due to nonsaturation in the resistance versus field measurement (maximum magnetic field ±25 mT). Interestingly, the effective anisotropy field H_A scales by about N/w in the linear regime [Fig. 3(b)]. This means that the linear magnetic field range can be widely tuned

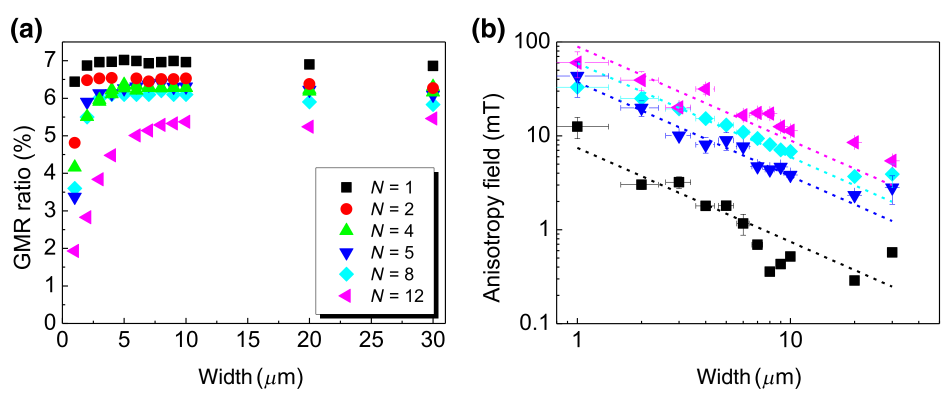

FIG. 3. (a) GMR ratio Δ_{GMR} and (b) effective anisotropy field as a function of width for yoke-shaped multi-GMR sensors ($N = 1$–12). The decrease in GMR ratio at low width is artificial and due to nonsaturation in resistance versus field measurements. Horizontal error bars represent the width sensor uncertainty from the microfabrication process (optical lithography and etching), while vertical error bars are absolute errors of the anisotropy calculation from two branches of the *R*-*H* curve (AP→P and P→AP, respectively). Dashed lines correspond to the analytical calculation from Eq. (1) using $M_s = 850$ kA/m and $t_{FL} = 7$ nm, respectively.

through N in multi-GMR sensors without modifying its area: up to 100 mT for $N = 12$ and $w = 1$ μm. The magnetic anisotropy field evolution can be explained by the dominant shape anisotropy ($H_{\rm SH}$) in patterned devices and can be approximated in multi-GMRs as

$$H_{\rm SH} = \mu_0 M_s \frac{N t_{\rm FL}}{w}, \tag{1}$$

where M_s is the saturation magnetization of the free layer. We find good agreement between the experimental effective anisotropy and Eq. (1), in particular, in the narrow width regime ($w < 10$ μm), where the shape anisotropy is dominant over the bulk magnetocrystalline anisotropy. At higher width, the effective anisotropy will reach a plateau given by the bulk magnetocrystalline anisotropy. Such analytical expression for multi-GMR is equivalent to the shape anisotropy in single GMRs [29], but taking into account the total free layer thickness, $N t_{\rm FL}$. However, compared with single GMRs, it is not possible to tune the magnetic field range in the same way through the Ni-Fe layer thickness. For a Ni-Fe layer thicker than 10 nm, the free layer is not uniform and the linearity and GMR ratio are strongly degraded (see Fig. S2 within the Supplemental Material [18]).

B. Micromagnetic simulations

To gain a better understanding of the correlation between the additive dipolar and Néel coupling with the magnetization reversal of multi-GMRs, we perform full micromagnetic simulations using OOMMF [22]. First, we compute the hysteresis loops under magnetic field H_x (along the pinned-layer magnetization direction) as a function of N and at constant width $w = 4$ μm [Fig. 2(d)]. The hysteresis loop is the total magnetization of the N free layers rotating from P ($\theta = \pi$) to AP ($\theta = 0$) configuration, $M_x = M_s \cos\theta = M_s \left[\left(\sum_{i=1}^{N} \cos\theta_i \right) / N \right]$, under the influence of external magnetic field, MC and shape anisotropies, and the Néel and dipolar couplings. And therefore the magnetoresistance of the sensor [Fig. (2c)] is directly proportional to the $\hat{x}$ component of total magnetization according to $R = R_0 + \Delta R \cos\theta = R_0 + (\Delta R / M_s) M_x$, where $R_0 = R(H_x = 0)$ and $\Delta R = (R_{\rm P} + R_{\rm AP})/2$. We can observe a very good agreement between the experiments and simulations. In particular, in Fig. 2, the simulations reproduce the evolution from steplike to linear behavior around $N = 5$. Notably, such transition can slightly vary, depending on the value of the uniaxial magnetic anisotropy constant K_u (magnetocrystalline anisotropy). Here, the best agreement with experiments is obtained for $K_u = 200$ J/m^3, which is coherent with the literature [23]: lower K_u values lead to lower threshold N and vice versa (not shown here). Moreover, the simulations also display that the effective anisotropy field scales with N in the linear region in good agreement with Fig. 3(b) and Eq. (1). In the simulations, we consider the Néel coupling distribution as an individual offset field in each free layer (H_{n1}, H_{n2},..., H_{nN}), taking into account the experimental results in Fig. 1.

To quantify the role of the two main couplings (additive dipolar versus Néel) in multi-GMRs, we repeat the same micromagnetic simulations without considering the Néel coupling distribution, that is, setting $H_{n1} = H_{n2} = \ldots = H_{nN} = 0$ (see Fig. S5 within the Supplemental Material [18]). We can observe that the yoke-shaped sensor exhibits very similar responses with and without Néel coupling distribution in the linear regime ($N \geq 5$), while differences are observed in the steplike regime ($N < 5$). The presence of the Néel coupling distribution increases the step length, that is, the separation between N individual jumps.

To shed more light on the magnetization rotation mechanism in multi-GMRs, we analyze the magnetization rotation of each individual free layer. Figure 4(a) displays the reversal magnetization of each free layer for a selected number of GMRs ($N = 2$, 4, and 8) with Néel coupling variation. Free layer 1 corresponds to the bottom layer with lowest roughness, while free layer N is the top layer with highest roughness. At double GMR $N = 2$, in the steplike regime, the magnetization rotation mechanism of the free layers is sequential: the first (second) layer rotates from P ($M_x = -1$) to AP ($M_x = +1$) configuration, while the second (first) is blocked in the P (AP) state. The sequential mode starts to vanish as N increases, leading to a more complex rotation scenario at $N = 4$. At higher $N = 8$, in the linear regime, all free layers rotate almost simultaneously in the same magnetic field range towards parallel rotation mode. Interestingly, the magnetic susceptibility of each free layer is strongly reduced in the parallel mode, but remains almost unaltered for the sequential mode.

The magnetization reversal of the layers is determined by competition between the different energies, anisotropies, and couplings. In particular, additive dipolar coupling between the free layers is antiferromagnetic and favors an antiparallel configuration between free layers [Fig. 4(b)]. The Néel coupling, as it is different for each free layer, breaks the symmetry of the system [Fig. 4(c)]. Due to Néel coupling, each free layer rotates at a different field. These two couplings, Néel and dipolar, explain the observed behavior in Figs. 4 and S5 within the Supplemental Material [18], respectively.

For $N = 2$, the Néel coupling favors the steplike behavior of the hysteresis cycle. Indeed, the free layer with the smallest Néel coupling rotates first and allows the antiferromagnetic configuration to be more stable than that without the Néel coupling. When N increases, a complex reversal of the layers, forming a spin-canted antiferromagnetic helix, appears. Due to Néel coupling, free layer 1, at the bottom, rotates first. Due to antiferromagnetic dipolar

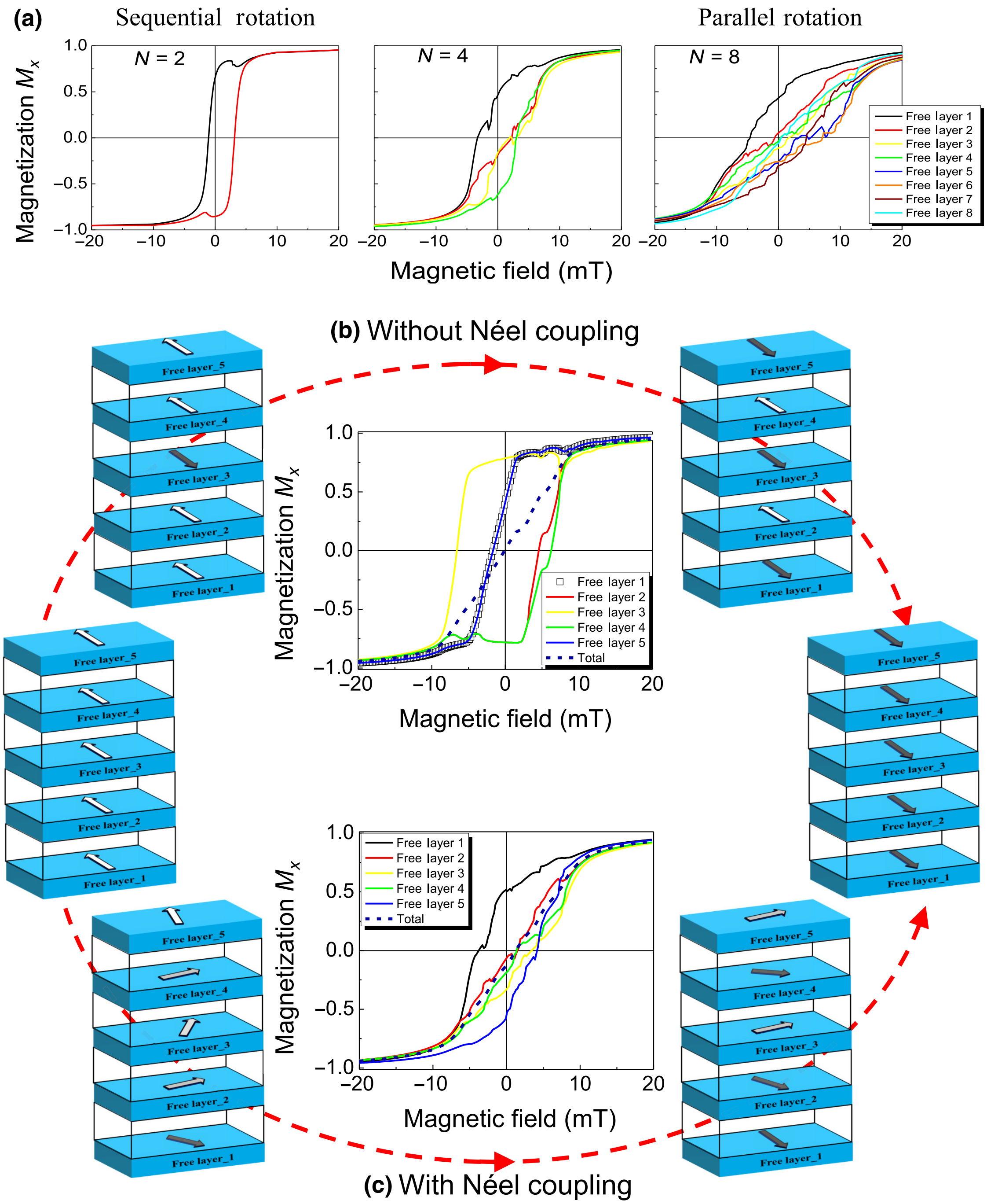

FIG. 4. Magnetization reversal of each individual free layer by OOMMF micromagnetic simulations. (a) Multi-GMR devices composed of 2, 4, and 8 GMRs with Néel coupling variation. (b),(c) Microdevice composed of 5 GMRs with and without Néel coupling variation. The Néel coupling distribution is simulated by different bias fields along the SAF pinned-layer direction ($H_{n1} = 0.8$ mT, $H_{n2} = 1.3$ mT, $H_{n3} = 1.4$ mT, $H_{n4} = 1.5$ mT, and $H_{n5} = H_{n6} = H_{n7} = H_{n8} = 1.6$ mT). Dimensions of the free layer are a rectangular prism of $200 \times 4 \times 0.007$ μm^3. We assume that Ni-Fe and Co-Fe layers are perfectly exchange coupled with the following magnetic parameters: saturation magnetization $M_s = 850$ kA/m, exchange constant $J_s = 10$ pJ/m, and weak uniaxial magnetic anisotropy $K_u = 200$ J/m^3. Gap (vertical separation) between consecutive free layers is 28 nm. External magnetic field along pinned-layer direction is swept between ± 20 mT.

coupling, a "spin-flop" rotation of the other free layers appears and creates, step by step, a complex antiferromagnetic helix rotation [Fig. 4(c)]. Without Néel coupling, the symmetry of the system is conserved and the free layers rotate in a more sequential mode [Fig. 4(b)]. For simplicity, we do not consider multidomain configurations for the interpretation of micromagnetic simulations in Fig. 4(b). Indeed, the single magnetic domain configuration approach describes reasonably well the complex magnetization reversal in multi-GMR in the strong dipolar range ($w \leq 5$ μm). However, the multidomain configuration should not be completely ruled out, in particular, in the weak dipolar range for wider devices.

In conclusion, the presence of Néel and dipolar couplings induces complex reversal behavior of the free layers. At low N, it favors a steplike resistance behavior, while, at higher N, a linearized multi-GMR response is observed with a spin-canted antiferromagnetic helix rotation.

V. MULTI-GMR SENSOR PERFORMANCE

In the last section, we characterize the multi-GMR sensor performance from noise measurements (Fig. 5) and extract the main parameters: sensitivity (s), noise (S_V), and detectivity ($D = S_V/sV_{\text{in}}$). The evolution of these sensor parameters with the number of GMR repetitions N, width, and input voltage (V_{in}) are correlated to the additive dipolar coupling, which is mainly characterized by N and w. For simplicity, experimental data for multi-GMRs $N = 2$ and $N = 5$ are not included in Fig. 6 and 7. Double GMRs exhibit a strong steplike behavior and remarkable RTN noise in many devices, and therefore, sensitivity and noise evolution differ from the general trend. Multi-GMRs with $N = 5$ exhibit very similar values to those of $N = 4$. Such additional data can be found in Fig. S6 within the Supplemental Material [18].

A. Sensitivity

Sensitivity is directly extracted from the reference ac magnetic signal at 30 Hz, which is basically the voltage amplitude divided by the equivalent field, $H_{\text{eq}} = 7$ μT, and input voltage, $V_{\text{in}} = 1$ V. The sensitivity of multi-GMRs as a function of width for selected $N = 1$, 4, 8, and 12 is displayed in Fig. 6(a). The sensitivity scales with the width when the shape anisotropy is the dominant mechanism in the narrow range and it is likely to be constant over the wide range, where the volume magnetocrystalline anisotropy overcomes the shape anisotropy. Interestingly, the linear evolution of sensitivity expands to a wider range as N increases: up to $w = 4$, 8, and 15 μm for $N = 4$, 8, and 12, respectively. As expected, the dipolar coupling is strongly correlated to the shape anisotropy because both are determined by the same parameters (width, thickness, and saturation magnetization of the free layer). Therefore, the number of GMR repetitions N plays a similar role to that of the thickness of the free layer, and the sensitivity in the strong dipolar regime (narrow range) decays roughly as N^{-1} [see dashed lines in Fig. 6(a)], according to the following expression:

$$s_{\text{dip}} = \left(\frac{\Delta_{\text{GMR}}}{2\mu_0 M_s t}\right)\frac{w}{N}. \tag{2}$$

Concerning the saturation range at wider width, the asymptotic sensitivity s_{MC} is very different between single GMR and multi-GMR. This might be ascribed to a change of effective magnetic (magnetocrystalline) anisotropy as a consequence of roughness propagation from the first to Nth free layer.

Finally, the sensitivity in the single GMR decays strongly for wider devices ($w \geq 10$ μm) because the offset field is close to the anisotropy field (magnetocrystalline contribution) and such devices operate close to the saturation regime similarly to the thin-film stack in the right-top panel in Fig. 1(b). In multi-GMR stacks, the additive dipolar coupling extends the range of maximum sensitivity around zero field (linearity) to wider range, but the same decays should be observed for wider devices than the maximum width analyzed in this study ($w > 30$ μm).

We should point out that the sensitivity can also be calculated from magnetotransport measurements in Figs. 2(b) and 2(c), when the R-H loops are practically anhysteretic. This is valid for narrow devices, where the sensitivity is just the resistance slope around zero magnetic field ($\pm$0.2 mT). As the hysteresis becomes noticeable at critical width, the sensitivity from magnetotransport deviates from those extracted from noise measurements and minor loops from irreversible mechanisms should be taken into account for the correct sensitivity estimation.

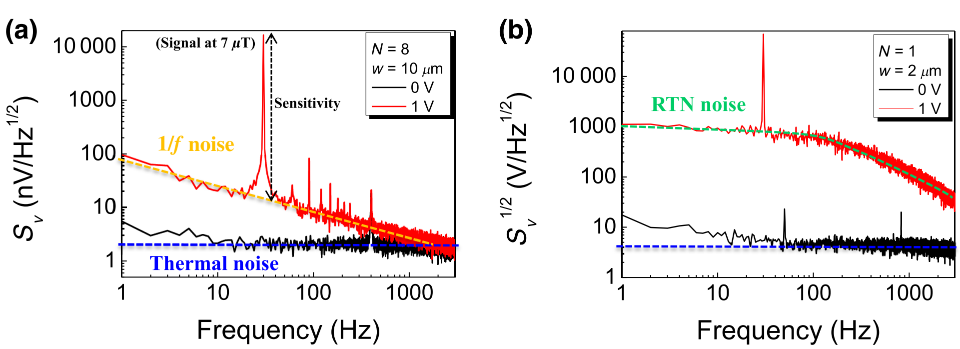

FIG. 5. Noise spectra in multi-GMR devices. Noise spectra of a multi-GMR sensor ($N = 8$, $w = 10$ μm) and (b) single GMR (N = 1 & w = 2 μm) consisting of different sources: $1/f$, thermal, and RTN noise. Higher frequency secondary peaks in (a) correspond to harmonics from the exciting ac magnetic field at 30 Hz.

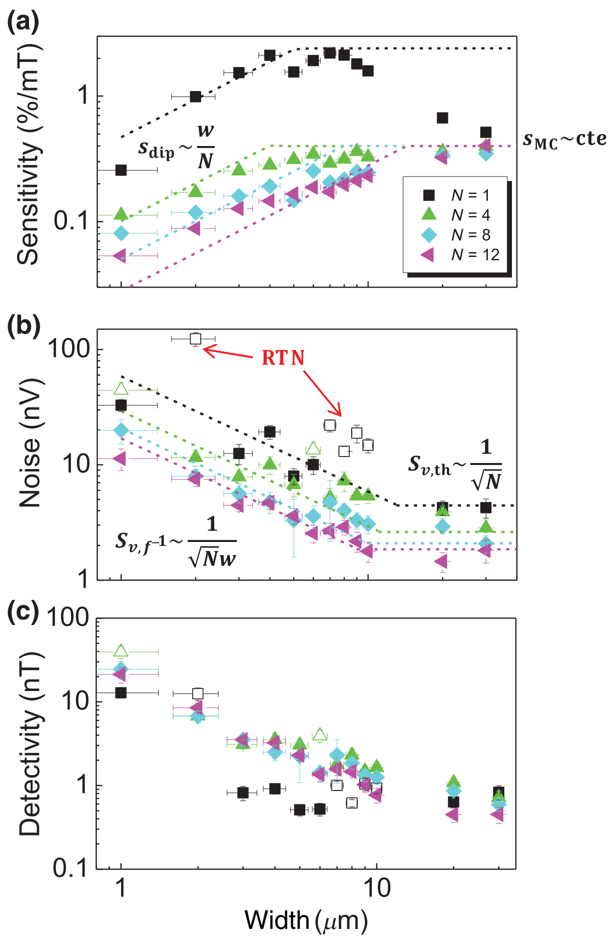

FIG. 6. Noise measurements in multi-GMR devices as a function of width for constant input voltage ($V_{\text{in}} = 1$ V). (a) Sensitivity, (b) noise (1 kHz), and (c) detectivity (1 kHz), as a function of the sensor width ($w = 1$–30 μm) for selected GMR numbers. Open symbols in (b) and (c) represent devices with large magnetic noise ($1/f$ or RTN). Horizontal error bars represent width sensor uncertainty from the microfabrication process (optical lithography and etching), while vertical error bars are standard deviations of the noise spectra. Dashed lines in (a) correspond to theoretical Eq. (2) with $M_s = 850$ kA/m, $t = 7$ nm and averaged GMR ratio for each multi-GMR system ($\Delta_{\text{GMR}} = 7\%$ for $N = 1$, $\Delta_{\text{GMR}} = 6\%$ for $N = 4$ and 8, and $\Delta_{\text{GMR}} = 5\%$ for $N = 12$), according to Fig. 3(a). Asymptotic sensitivities, s_{MC}, are manually added in (a) for better visualization. Dashed lines in (b) correspond to theoretical fit from Eq. (3) in the $1/f$ regime and Eq. (4) in the thermal regime using average $\alpha = 1.2 \times 10^{-12}$ μm^3 for all devices, single GMR resistance $R_1 = 800\,\Omega$, and temperature $T = 300$ K. A vertical offset of 0.8 nV is added in the thermal regime to take into account the noise floor of the experimental setup.

B. Noise

The power spectral density S_V [Figs. 5(a) and 5(b)] associated with the noise in GMR sensors can exhibit different origins [30]: $1/f$ ($S_{V,f^{-1}}$) and thermal noise ($S_{V,\text{th}}$) and, in some cases, undesirable Lorentzian RTN ($S_{V,\text{RTN}}$). In the absence of RTN, the noise is dominated by $1/f$ noise at low frequencies and thermal noise at high frequencies [Fig. 5(a)]. In particular, for a multi-GMR with $N = 8$ and $w = 10$ μm, the $1/f$ noise is found below 2 kHz and the thermal noise above this corner frequency. The noise level at 1 kHz of multi-GMR sensors ($N = 1$, 4, 8, and 12) as a function of the width and for a constant input voltage $V_{\text{in}} = 1$ V is shown in Fig. 6(b). For $w \leq 10$ μm, the sensors are in the $1/f$ regime and the noise level decreases with the magnetic volume of the free magnetic layer by

$$S_{v,f^{-1}} = \sqrt{\frac{\alpha}{V_{\text{FL}} f}} V_{\text{in}} = \sqrt{\frac{\alpha}{50 N t f}} \frac{V_{\text{in}}}{w}, \tag{3}$$

where α is the Hooge constant and it can have electric and magnetic origins. It is a very relevant parameter when comparing the performance of different magnetic systems. The yoke-shaped sensors have the same aspect ratio, $L = 50\,w$, and the total magnetic thickness is $N t_{\text{FL}}$, then the noise in Fig. 6(b) decreases in the $1/f$ regime by about $1/\sqrt{N}w$, which is in reasonably good agreement with Eq. (3) using the same Hooge constant of $\alpha = 1.2 \times 10^{-12}$ μm^3 for all devices. Nevertheless, some devices deviate from Eq. (3) due to the presence of large magnetic noise at low frequency ($1/f$ or RTN) induced by magnetic fluctuations in the free layer(s), and therefore, increasing drastically α (the magnetic origin). The magnetic noise ($1/f$ or RTN) is noticeable in a single GMR with very weak shape anisotropy ($w = 6$–10 μm) and multi-GMRs with weak dipolar coupling $N \leq 4$. Magnetic noise is rarely observed in narrow devices with strong shape anisotropy [single GMR, $w = 2$ μm, Fig. 5(b)], which might be due to some defects created during the microfabrication process (in particular, during the etching process) that might act as a seed of reversed domains nucleation [31]. However, for multi-GMRs with $N > 4$, the magnetic noise and RTN is not observed in the full width and voltage range (up to 3 V). An explanation is that the increased dipolar coupling stabilizes the magnetic domains and suppresses magnetic noise.

For $w > 10$ μm, the sensors reach the thermal regime, where the noise depends only on the total resistance of the devices according to

$$S_{v,\text{th}} = \sqrt{4 k_B T R_N} = \sqrt{\frac{4 k_B T R_1}{N}}. \tag{4}$$

Each GMR repetition reduces the total resistance, according to $R_N = R_1/N$. Therefore, the thermal noise in Fig. 6(b) is roughly reduced by $\sqrt{N}$. Notably, Eq. (4) provides lower noise levels than that of experiments because the current and voltage input noise of the preamplifier have to be added quadratically.

C. Detectivity

Finally, the magnetic field detectivity, D, of multi-GMR sensors is evaluated as a function of width [Fig. 6(c)] and

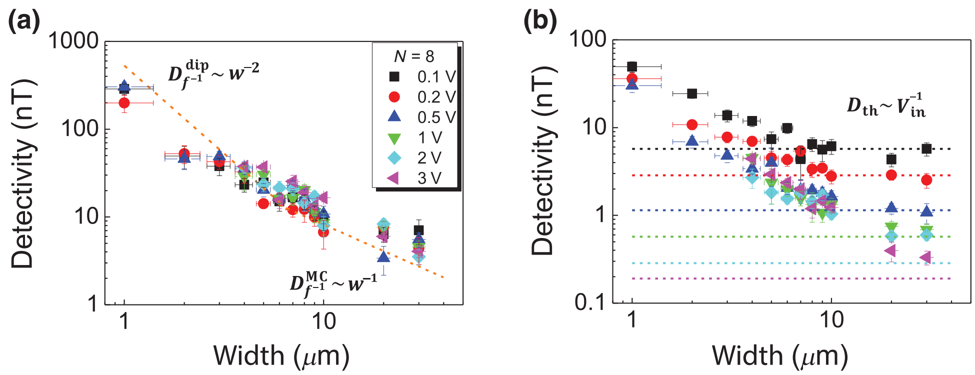

FIG. 7. Detectivity evolution with input voltage. Detectivity as a function of sensor width for selected input voltage range (0.1–3 V) for a sensor composed of eight GMRs for two different frequencies: (a) 10 Hz and (b) 1 kHz. Horizontal error bars represent width sensor uncertainty from the microfabrication process (optical lithography and etching), while vertical error bars are standard deviations of the noise spectra. Dashed guidelines are manually added for better visualization. Dashed lines in (a) correspond to theoretical fits from Eq. (5) for $= 2 \times 10^{-12}\ \mu m^3$ in the narrow range ($\Delta_{GMR} = 6\%$, $M_s = 850$ kA/m, and $t = 7$ nm) and Eq. (6) for $= 3 \times 10^{-12}\ \mu m^3$ in the wide range (asymptotic sensitivity $s_{MC} = 0.4\%$/mT). Dashed lines in (b) correspond to theoretical fit from Eq. (7) using single GMR resistance $R_1 = 800\ \Omega$ and temperature $T = 300$ K. A residual noise floor of 1 nV is taken into account in the thermal regime.

input voltage (Figs. 7). The detectivity evolution at 1 kHz with the width in Fig. 6(c) reflects the complex competition between sensitivity (both components, dipolar s_{dip} and magnetocrystalline s_{MC}) and noise (both regimes, $1/f$ and thermal), according to $D = (S_V/sV_{in})$. Indeed, a multi-GMR could be in four regimes. At low width and low frequencies, the dipolar coupling and $1/f$ noise dominate the sensitivity and noise behavior, respectively. The detectivity (without considering RTN) scales as about $\sqrt{N}/w^2$, according to

$$D^{dip}_{f^{-1}} = \frac{S_{v,f^{-1}}}{s_{dip}V_{in}} = \left(\frac{2\mu_0 M_s\sqrt{\alpha t}}{\Delta_{GMR}\sqrt{50f}}\right)\frac{\sqrt{N}}{w^2}. \quad (5)$$

At higher width and low frequencies, the magnetocrystalline anisotropy overcomes the shape anisotropy, so s_{MC} should be considered instead of s_{dip}, and the detectivity decays slower by about w^{-1} according to

$$D^{MC}_{f^{-1}} = \frac{S_{v,f^{-1}}}{s_{MC}V_{in}} = \sqrt{\frac{\alpha}{50Ntf}}\frac{1}{s_{MC}w}. \quad (6)$$

At higher width ($w \geq 10\ \mu$m) and high frequencies (in the thermal regime), the dipolar coupling is negligible, magnetocrystalline anisotropy dominates, and sensitivity converges to a constant value of s_{MC}. Therefore, the detectivity in the thermal regime is independent of the width scaling as $1/\sqrt{N}$, according to

$$D_{th} = \frac{S_{v,th}}{s_{MC}V_{in}} = \sqrt{\frac{4k_B TR_1}{N}}\frac{1}{s_{MC}V_{in}}. \quad (7)$$

The last regime, low width and high frequencies, is not investigated here, since the frequency (∼MHz) has to be very high to achieve the thermal regime.

In general, the single GMR exhibits a better detectivity in the narrow width range ($w \leq 8\ \mu$m), while multi-GMR performance is more competitive in the large width range ($w \geq 10\ \mu$m); this is in good qualitative agreement with Eqs. (5)–(7). The $1/f$ detectivity variation for single GMRs does not follow Eq. (6) due to presence of a remarkable RTN in the intermediate width range ($w = 7$–$10\ \mu$m). Despite the remarkable magnetic noise and RTN of the single GMR, its much higher asymptotic sensitivity, s_{MC}, still leads to lower or similar detectivity levels to that of the multi-GMR sensor in the intermediate width range.

For input voltages above 1 V, the detectivity of single GMRs is strongly degraded by the presence of a remarkable RTN. The multi-GMR is more robust against magnetic noise, and RTN is not observed for $N > 4$ (in the full width range) up to a maximum input voltage of 3 V, as shown Fig. 7. Above 3 V, the high current density heats the stacks, leading to a progressive decrease in the sensitivity (not shown here). The detectivity for a multi-GMR with $N = 8$ is analyzed over an input voltage range between 0.1 and 3 V (Fig. 7). In the $1/f$ noise regime at 10 Hz [Fig. 7(a)], the detectivity is constant with the input voltage and exhibits two different contributions ($D^{dip}_{f^{-1}}$ and $D^{MC}_{f^{-1}}$), according to Eqs. (5) and (6). Good agreement between experiments and theory in Fig. 7(a) is obtained for $\alpha = 2 \times 10^{-12}\ \mu m^3$ in the dipolar regime and $\alpha = 3 \times 10^{-12}\ \mu m^3$ in the magnetocrystalline regime. This result suggests that α can also vary between devices with different widths in the same multi-GMR systems and be a possible source of discrepancies between theory and experiments in Figs. 6(b) and 7(a). In particular, the hysteresis is more relevant in wider devices, leading, in general, to higher magnetic noise, and therefore, higher α.

Finally, the detectivity is reduced roughly by V_{in}^{-1} in the thermal regime at 1 kHz [Fig. 7(b)], in good agreement with Eq. (7). Notably, the threshold width for reaching the thermal regime depends on the voltage, and higher voltages shift the $1/f$ thermal transition to wider widths: from w_c ~6 to 20 μm, when voltage increases from 0.1 to 3 V, respectively. Similarly to Fig. 6(b), additional residual noise of about 1 nV is needed to observe good quantitative agreement between experiments and theory. Discrepancies at maximum voltages might be ascribed to progressive heating of the multi-GMR stacks, leading to a progressive reduction of sensitivity and/or an increase in thermal noise (through the temperature).

VI. CONCLUSION

All important considerations for multi-GMR sensors are highlighted in Table I. In summary, we fabricate and characterize (from magnetotransport and noise measurements) multi-GMR sensors based on N (up to 12) spin valves vertically stacked, which retain a good GMR ratio, linearity, and low roughness propagation. Combining magnetoresistance measurements with micromagnetic simulations, we identify the two main magnetic mechanisms: Néel coupling distribution, which is induced by roughness propagation, and additive dipolar coupling between the free layers. From experiments, we find a smooth crossover from steplike to linear behavior at $N = 5$ ($w = 4$ μm), which is in excellent agreement with micromagnetic simulations. At low N, a steplike response is stabilized by the combination of both additive dipolar and Néel couplings, where the reversal magnetization of the N dipolar-coupled free layers is likely to be sequential, maintaining antiferromagnetic order at zero field. As N increases, the Néel coupling variation between the free layers induces a more complex reversal in a spin-canted antiferromagnetic helix, resulting in a linearization of the resistance response.

Compared with single GMRs for weak magnetic-field-sensing applications, multi-GMR sensor performance exhibits very good linearity over a much larger magnetic field range (one order of magnitude larger, up to $\pm$100 mT) without remarkable degradation of the GMR ratio, with a noise reduction of about $1/\sqrt{N}$ in both $1/f$ (via magnetic volume) and thermal (through the total resistance) regimes and with more robustness against magnetic noise ($1/f$ and/or RTN). However, the sensitivity roughly decreases by N^{-1} due to the strong dipolar coupling between neighboring free layers, and it has a negative impact on the detectivity at the $1/f$ noise regime. Therefore, lower detectivities in multi-GMRs are only achieved in the thermal regime for the widest devices with negligible dipolar coupling. Finally, the analytical equations predict reasonably well the experimental evolution of sensitivity and noise with number of GMR repetitions, width, and input voltage and can be used as general guidelines to design multi-GMR sensors with optimized performance.

These results for multi-GMR stack opens a route towards spintronic sensors coupled in three dimensions with a compact footprint and additional tunable parameters through the number of vertically stacked GMRs (N). The next generation of multi-GMR sensors with improved detectivity will need to overcome some fabrication challenges to minimize sensitivity loss (induced by dipolar coupling): increasing the spacer thickness and number of GMRs, avoiding a strong roughness degradation and a very long fabrication process, and/or growing multi-GMR stacks based on synthetic antiferromagnetic free layers [32] without a remarkable degradation of GMR ratio, linearity, and offset. Furthermore, we anticipate that three-dimensional (3D) stacking for a reduction of low-frequency noise is also of interest for sensors based on tunnel magnetoresistance (TMR). Relative to GMRs, TMRs have an enhanced MR ratio, which is counterbalanced by much larger low-frequency noise levels [30]. For noise-reduction 3D stacking, however, the influence of

TABLE I. Main relevant points of multi-GMR sensor performance compared with a single GMR, in terms of GMR ratio, roughness, linearity, sensitivity, noise, and detectivity.

	Multi-GMR based on N spin valves	Single GMR
GMR ratio	Smooth decrease from 7% to 6% for max $N = 12$	7%
Roughness	Low roughness propagation up to $N = 12$	Offset < 0.8 mT
(Néel coupling)	(max offset ~3 mT at $N = 12$)	
Linearity	Tuned by N in a large magnetic field range	Limited to few mT
	(up to $\pm$100 mT for $N = 12$ and $w = 1$ μm)	($\pm$10 mT for $w = 1$ μm)
Sensitivity	Decreases by about N^{-1} (strong dipolar regime)	Max $s \sim 2$ %/mT
	Converges to $s \sim 0.4$ %/mT (weak dipolar regime)	($w = 4$–10 μm)
Noise	Decreases by about $1/\sqrt{N}$ in the $1/f$ and thermal regime	Stronger magnetic noise
	Robust against RTN for $N > 4$ up to 3 V in full width range	($w = 6$–10 μm, $V_{\text{in}} \geq 1$V)
Detectivity	Higher in the $1/f$, $D \sim \sqrt{N}$	Optimal D for $V_{\text{in}} \leq 1$ V
	Lower in the thermal regime at high V_{in}	

roughness propagation on stacked TMRs remains an open question.

ACKNOWLEDGMENTS

This research is supported by the Agence Nationale de Recherche (France) through Grant No. ANR-17-CE19-0021-01 (NeuroTMR) and the Commissariat à l'énergie atomique et aux énergies alternatives (CEA) for the internally funded project CARAMEL. A.D. acknowledges a SNSF mobility fellowship (177732).

[1] M. Baibich, J. Broto, A. Fert, F. Nguyen Van Dau, F. Petroff, P. Etienne, G. Creuzet, A. Friederich, and J. Chazelas, Giant Magnetoresistance of (001)Fe/(001)Cr Magnetic Superlattices, Phys. Rev. Lett. **61**, 2472 (1988).

[2] G. Binasch, P. Grünberg, F. Saurenbach, and W. Zinn, Enhanced magnetoresistance in layered magnetic structures with antiferromagnetic interlayer exchange, Phys. Rev. B **39**, 4828 (1989).

[3] C. Reig, S. Cardoso de Freitas, and S. Chandra Mukhopadhyay, *Giant Magnetoresistance (GMR) Sensors* (Springer-Verlag, Berlin, Heidelberg, 2013).

[4] P. Campiglio and C. Fermon, *Large-Volume Applications of Spin Electronics Based Sensors in Nanomagnetism: Applications and Perspectives* (Wiley-VCH, Weinheim, 2017).

[5] L. Caruso, T. Wunderle, C. M. Lewis, J. Valadeiro, V. Trauchessec, J. Trejo Rosillo, J. P. Amaral, J. Ni, P. Jendritza, C. Fermon, S. Cardoso, P. P. Freitas, P. Fries, and M. Pannetier-Lecoeur, In vivo magnetic recording of neuronal activity, Neuron **95**, 1283 (2017).

[6] F. Barbieri, V. Trauchessec, L. Caruso, J. Trejo-Rosillo, B. Telenczuk, E. Paul, T. Bal, A. Destexhe, C. Fermon, M. Pannetier-Lecoeur, and G. Ouanounou, Local recording of biological magnetic fields using Giant Magneto Resistance-based micro-probes, Sci. Rep. **6**, 39330 (2016).

[7] F. N. Hooge, 1/f noise is no surface effect, Phys. Lett. A **29**, 139 (1969).

[8] P. Dutta and P. M. Horn, Low-frequency fluctuations in solids: 1/f noise, Rev. Mod. Phys. **53**, 497 (1981).

[9] A. Ozbay, A. Gokce, T. Flanagan, R. A. Stearrett, E. R. Nowak, and C. Nordman, Low frequency magnetoresistive noise in spin-valve structures, Appl. Phys. Lett. **94**, 202506 (2009).

[10] A. Guedes, J. M. Almeida, S. Cardoso, R. Ferreira, and P. P. Freitas, Improving magnetic field detection limits of spin valve sensors using magnetic flux guide concentrators, IEEE Trans. Magn. **43**, 2376 (2007).

[11] E. Paz, S. Serrano-Guisan, R. Ferreira, and P. P. Freitas, Room temperature direct detection of low frequency magnetic fields in the 100 pT/Hz$^{0.5}$ range using large arrays of magnetic tunnel junctions, J. Appl. Phys. **115**, 17E501 (2014).

[12] L. Huang, Z. H. Yuan, B. S. Tao, C. H. Wan, P. Guo, Q. T. Zhang, L. Yin, J. F. Feng, T. Nakano, H. Naganuma, H. F. Liu, Y. Yan, and X. F. Han, Noise suppression and sensitivity manipulation of magnetic tunnel junction sensors with soft magnetic Co70.5Fe4.5Si15B10 layer, J. Appl. Phys. **122**, 113903 (2017).

[13] P. Wisniowski, M. Dąbek, W. Skowronski, T. Stobiecki, S. Cardoso, and P. P. Freitas, Reduction of low frequency magnetic noise by voltage-induced magnetic anisotropy modulation in tunneling magnetoresistance sensors, Appl. Phys. Lett. **105**, 082404 (2014).

[14] D. Mazumdar, X. Liu, B. D. Schrag, M. Carter, W. Shen, and G. Xiao, Low frequency noise in highly sensitive magnetic tunnel junctions with (001) MgO tunnel barrier, Appl. Phys. Lett. **91**, 033507 (2007).

[15] S. Ingvarsson, G. Xiao, S. S. P. Parkin, W. J. Gallagher, G. Grinstein, and R. H. Koch, Low-Frequency Magnetic Noise in Micron-Scale Magnetic Tunnel Junctions, Phys. Rev. Lett. **85**, 3289 (2000).

[16] J. Moulin, A. Doll, E. Paul, M. Pannetier-Lecoeur, C. Fermon, N. Sergeeva-Chollet, and A. Solignac, Optimizing magnetoresistive sensor signal-to-noise via pinning field tuning, Appl. Phys. Lett. **115**, 122406 (2019).

[17] M. Silva, D. C. Leitao, S. Cardoso, and P. P. Freitas, Toward pTesla detectivities maintaining minimum sensor footprint with vertical packaging of spin valves, IEEE Trans. Magn. **53**, 1 (2017).

[18] See the Supplemental Material at https://link.aps.org/supplemental/10.1103/PhysRevApplied.13.034031 for Supplementary Figures S1–S6.

[19] J. Y. Chen, N. Carroll, J. F. Feng, and J. M. D. Coey, Yoke-shaped MgO-barrier magnetic tunnel junction sensors, Appl. Phys. Lett. **101**, 262402 (2012).

[20] M. Pannetier, C. Fermon, G. Le Goff, J. Simola, and E. Kerr, Femtotesla magnetic field measurement with magnetoresistive sensors, Science **304**, 1648 (2004).

[21] C. Fermon, M. Pannetier-Lecoeur, N. Biziere, and B. Cousin, Optimised GMR sensors for low and high frequencies applications, Sens. Actuators A Phys. **129**, 203 (2006).

[22] M. Donahue and D. Porter, *OOMMF User's Guid. Version 1.0* (Interag. Rep. NISTIR 6376, NIST, Gaithersburg, MD, 1999).

[23] S. Ingvarsson, G. Xiao, S. S. P. Parkin, and W. J. Gallagher, Thickness-dependent magnetic properties of Ni81Fe19, Co90Fe10 and Ni65Fe15Co20 thin films, J. Magn. Magn. Mater. **251**, 202 (2002).

[24] P. Bruno and C. Chappert, Oscillatory Coupling Between Ferromagnetic Layers Separated by a Nonmagnetic Metal Spacer, Phys. Rev. Lett. **67**, 1602 (1991).

[25] P. Bruno, Theory of interlayer magnetic coupling, Phys. Rev. B **52**, 411 (1995).

[26] C.-L. Lee, J. A. Bain, S. Chu, and M. E. McHenry, Separation of contributions to spin valve interlayer exchange coupling field by temperature dependent coupling field measurements, J. Appl. Phys. **91**, 7113 (2002).

[27] J. M. Teixeira, J. O. Ventura, R. P. Fermento, J. P. Araújo, J. B. Sousa, S. C. Freitas, and P. J. Freitas, Interlayer coupling and magnetoresistance of MnIr-based spin valves: Dependencies on deposition rate, spacer thickness, and temperature, IEEE Trans. Magn. **43**, 3143 (2007).

[28] A. V. Silva, D. C. Leitao, J. Valadeiro, J. Amaral, P. P. Freitas, and S. Cardoso, Linearization strategies for high sensitivity magnetoresistive sensors, EPJ Appl. Phys. **72**, 10601 (2015).

[29] Z. Qian, R. Bai, C. Yang, Q. Li, Y. Sun, D. Huo, L. Li, H. Zhan, Y. Li, and J. Zhu, Effective anisotropy field in the free layer of patterned spin-valve resistors, J. Appl. Phys. **109**, 103904 (2011).

[30] C. Fermon and M. Pannetier-Lecoeur, *Noise in GMR and TMR Sensors in Giant Magnetoresistance Sensors* (Springer-Verlag, Berlin, Heidelberg, 2013).

[31] R. P. Cowburn, J. Ferré, S. J. Gray, and J. A. C. Bland, Domain-wall dynamics, pinning, and nucleation in ultrathin epitaxial Fe films, Phys. Rev. B **58**, 11507 (1998).

[32] A. Veloso and P. P. Freitas, Spin valve sensors with synthetic free and pinned layers, J. Appl. Phys. **87**, 5744 (2000).